


3D-PRINTED ELECTRODES FOR ENERGY STORAGE



Microstructure, mechanical properties, and ionic conductivity of a solid-state electrolyte prepared using binderless laser powder bed fusion

Katherine A. Acord¹, Alexander D. Dupuy¹, Xin Wang¹, Alexandra L. Vyatskikh¹, Olivia K. Donaldson¹, Timothy J. Rupert¹, James J. Wu², Qian Nataly Chen³, Julie M. Schoenung^{1,a)} 

¹Department of Materials Science and Engineering, University of California, Irvine, 716B Engineering Tower, Irvine, CA 92697, USA

²NASA Glenn Research Center, 21000 Brookpark Road, Cleveland, OH 44135, USA

³Jet Propulsion Laboratory, California Institute of Technology, 4800 Oak Grove Drive, Pasadena, CA 91109, USA

^{a)}Address all correspondence to this author. e-mail: Julie.Schoenung@uci.edu

Received: 7 July 2021; accepted: 13 September 2021

Timothy J. Rupert was an editor of this journal during the review and decision stage. For the JMR policy on review and publication of manuscripts authored by editors, please refer to <http://www.mrs.org/editor-manuscripts/>.

Manipulating the microstructure of the glass–ceramic solid-state electrolyte $\text{Li}_{1+x}\text{Al}_x\text{Ti}_{2-x}(\text{PO}_4)_3$ (LATP) improves performance by enhancing ionic conductivity; however, conventional glass–ceramic processing requires multiple processing steps to successfully develop the microstructure. Laser-based additive manufacturing techniques, such as laser powder bed fusion (L-PBF), offer a novel approach to single-step fabrication of glass–ceramics for battery applications. Here, we investigate the influence of L-PBF processing on the microstructure, mechanical properties, and ionic conductivity of LATP. This study demonstrates that binderless L-PBF produces relatively dense LATP samples (up to ~96% dense) with the desired rhombohedral crystal structure and mechanical properties consistent with conventional LATP. We find that laser scan speed influences the development of secondary phase particles, which affect the ionic conductivity. Further parameter optimization will improve the ionic conductivity of L-PBF LATP to enable single-step fabrication of LATP as a solid-state battery electrolyte using binderless laser-based additive manufacturing.

Introduction

Solid-state batteries offer enhanced safety and performance over batteries with flammable liquid electrolytes; however, improvements to the ionic conductivity of the solid-state electrolytes are necessary for widespread adoption. Solid-state electrolyte $\text{Li}_{1+x}\text{Al}_x\text{Ti}_{2-x}(\text{PO}_4)_3$ (LATP) glass–ceramics are typically prepared using the two-step glass–ceramic process where the glass is formed through splat-quenching and then crystallized through controlled high-temperature heat treatments [1]. Modification of the microstructure of LATP has proven useful for enhancing room temperature ionic conductivity by approximately four orders of magnitude (from $\sim 10^{-7}$ to $\sim 10^{-3}$ S cm⁻¹) [1]. Ionic conductivity of LATP depends on the density and

grain size, which are influenced by the heat treatment time and temperature [1]. Increasing the density and grain size of LATP by increasing the heat treatment temperature improves the ionic conductivity [1]. However, there is a limit to this behavior. Higher heat treatment temperatures can cause significant secondary phase segregation that lowers the ionic conductivity [1, 2]. Moreover, LATP samples exhibit a higher propensity for crack formation once average grain sizes increase to larger than ~ 2 μm , which jeopardizes the structural stability and reduces the ionic conductivity [3]. The propensity for crack formation depends on mechanical properties, such as Young's modulus and fracture toughness [3]. These mechanical properties are critical in inhibiting the nucleation of lithium dendrites

from lithium-metal anodes, which lead to short circuiting of solid-state lithium-metal-based batteries [4]. However, the current methods used to produce bulk glass-ceramic LATP samples involve multi-step processes that offer limited potential for extending the microstructural control of solid-state electrolytes [1]. The laser-based additive manufacturing (AM) technique, laser powder bed fusion (L-PBF), can be used to address these challenges, as it enables microstructural engineering and extended geometric complexity.

L-PBF is an AM technique that has been explored for binderless fabrication of glasses and ceramics. During L-PBF, the layer-by-layer consolidation of material leads to iterative heating and cooling cycles that can result in crack formation in brittle material systems, such as ceramics and glasses. Most of the research has therefore focused on a narrow set of ceramic materials, including Al_2O_3 , ZrO_2 , and yttrium aluminum garnet (YAG) [5–10]. Findings show that utilizing lower temperature eutectics limits crack formation and produces unique fine scale (or sub-micron) microstructural features in ceramics [10]. When eutectics are not achievable, secondary lasers have been used to preheat the powder bed ahead of the consolidation laser to reduce thermal gradients, promoting densification and reducing the propensity for crack formation [5]. While AM of ceramics and glasses has been demonstrated with some success, little work exists for AM of glass-ceramics. Moreover, the previous work on AM has focused on investigating the relationship between process parameters and structural integrity rather than on mechanical and functional properties.

Binderless L-PBF offers a novel approach for single-step fabrication of glass-ceramics. During L-PBF, a high-energy laser rasters over a bed of powder to melt and consolidate specific regions of the powder bed according to a computer aided design (CAD) model [11]. Once the two-dimensional slice of the three-dimensional CAD model is deposited, the laser head raises in the z-axis (i.e., along the build direction) to accommodate the fresh bed of powder. The previously deposited layers then undergo reheating as new layers of material are added, leading to a unique thermal history within L-PBF components. We hypothesize that the unique thermal history produced during L-PBF can be uniquely beneficial for single-step fabrication of functional glass-ceramics. For instance, the cooling rates produced during the initial melt and consolidation step of L-PBF (10^3 – 10^4 K sec^{-1} [12]) are high enough to enable glass formation [13]. Although crystallization of glass has not been demonstrated during the reheating cycle of L-PBF, Pang et al. [14] show that laser-induced crystallization of LATP glass improves the ionic conductivity. Since the performance of LATP greatly depends on microstructural features, such as average grain size, porosity, and secondary phase content, utilizing binderless L-PBF for single-step glass-ceramic processing has the potential

to further improve the performance through microstructural engineering of LATP.

Process parameters, such as laser scan speed [15] and laser power [16], can influence the microstructural features that develop during L-PBF. Since materials undergo melting and solidification during L-PBF, the key solidification parameters, temperature gradient (G) and the solidification rate (R), dictate the resulting microstructural features [17]. The cooling rate ($G \cdot R$) determines the size of the microstructural features, whereas the ratio (G/R) controls the type of solidification structure that will develop (e.g., planar, cellular, columnar dendritic, etc.) [17]. The L-PBF process parameter, laser scan speed, directly influences these key solidification parameters. For instance, increasing the laser scan speed increases the solidification rate and cooling rate, which, in turn, decrease the average grain size [15]. However, high laser scan speed may lead to an unstable melt pool that produces porosity and lowers the relative density of the L-PBF fabricated part [18]. Moreover, the laser scan speed influences the G/R ratio, leading to transitions between regular and irregular solidification structures under varying laser scan speeds [10]. Therefore, the laser scan speed is crucial for engineering the microstructure of materials during L-PBF.

Considering the above review of the literature, the goal of this study is to enable single-step fabrication of functional glass-ceramic LATP samples using binderless L-PBF (denoted hereafter as L-PBF LATP samples). While variation in laser scan speed and laser power are both expected to influence the microstructure of L-PBF LATP samples, the lowest available laser power (100 W) was employed in this study to minimize materials decomposition during processing, and laser scan speed was selected as the L-PBF process parameter of interest. Therefore, this study will determine the relationship between a key L-PBF process parameter, laser scan speed, and the microstructure, mechanical, and electrical properties (i.e., ionic conductivity, electronic conductivity, dielectric constant) of the L-PBF LATP samples. We find that the L-PBF LATP samples exhibit relative density values (up to ~96% dense) and mechanical property values, including Young's modulus and hardness, that are comparable to literature values for conventionally prepared glass-ceramic LATP. Additionally, we demonstrate that the secondary phase content depends on laser scan speed and influences the ionic conductivity. This study identifies laser scan speed as an important L-PBF process parameter that is useful in engineering microstructural features to improve the ionic conductivity of the L-PBF LATP samples. The binderless L-PBF for single-step glass-ceramic processing developed in this work constitutes a novel facile approach for controlling the microstructure of solid-state electrolytes to improve their performance.

Results

First, we characterized the LATP feedstock powder. The morphology of the as-received LATP (AR-LATP) powder is displayed in Fig. 1. The AR-LATP secondary powder particles are comprised of agglomerated primary powder particles. The scanning electron microscopy (SEM) micrographs of the AR-LATP powder reveal oblong secondary particles (Fig. 1a) composed of cubic primary particles (Fig. 1b). The X-ray diffraction (XRD) pattern of the AR-LATP powder (Fig. 1c) was indexed to the expected rhombohedral crystal structure (space group R-3c) from the reference diffraction pattern ICSD PDF: 01-072-6140. Figure 1d displays a model of the AR-LATP crystal structure [19].

Next, characterization of the as-prepared L-PBF LATP samples was performed. A representative, as-prepared L-PBF LATP sample, shown in Fig. 2a, is consistent with the CAD-specified cylindrical geometry and dimensions. The top surface of the as-prepared L-PBF LATP sample is violet in color and features artifacts from the laser scan pattern. The edges of the as-prepared

L-PBF LATP sample are white due to unmelted powder particles that adhered to the sample from the powder bed. The polished cross-section of the L-PBF LATP sample, shown in Fig. 2b, reveals the clamshell shape of the solidified melt pool, as well as processing defects, such as cracks (orange arrows) and pores (black arrows).

The relative density values and average grain size of the L-PBF LATP samples are provided as a function of laser scan speed in Table 1. The highest laser scan speed, 13.5 mm s^{-1} , has the highest relative density values, $95.9 \pm 5.2\%$, and largest average grain size values, $1.58 \pm 1.11 \mu\text{m}$. The relative density and average grain size do not exhibit a specific trend with laser scan speed, likely due to large variability in the concentration of processing defects that arise from the stochastic nature of the L-PBF process [20] and the implementation of a custom powder bed setup.

The microstructure was further characterized using SEM, scanning transmission electron microscopy (STEM), and energy dispersive X-ray spectroscopy (EDS). The representative backscattered electron (BSE) SEM micrographs reveal the

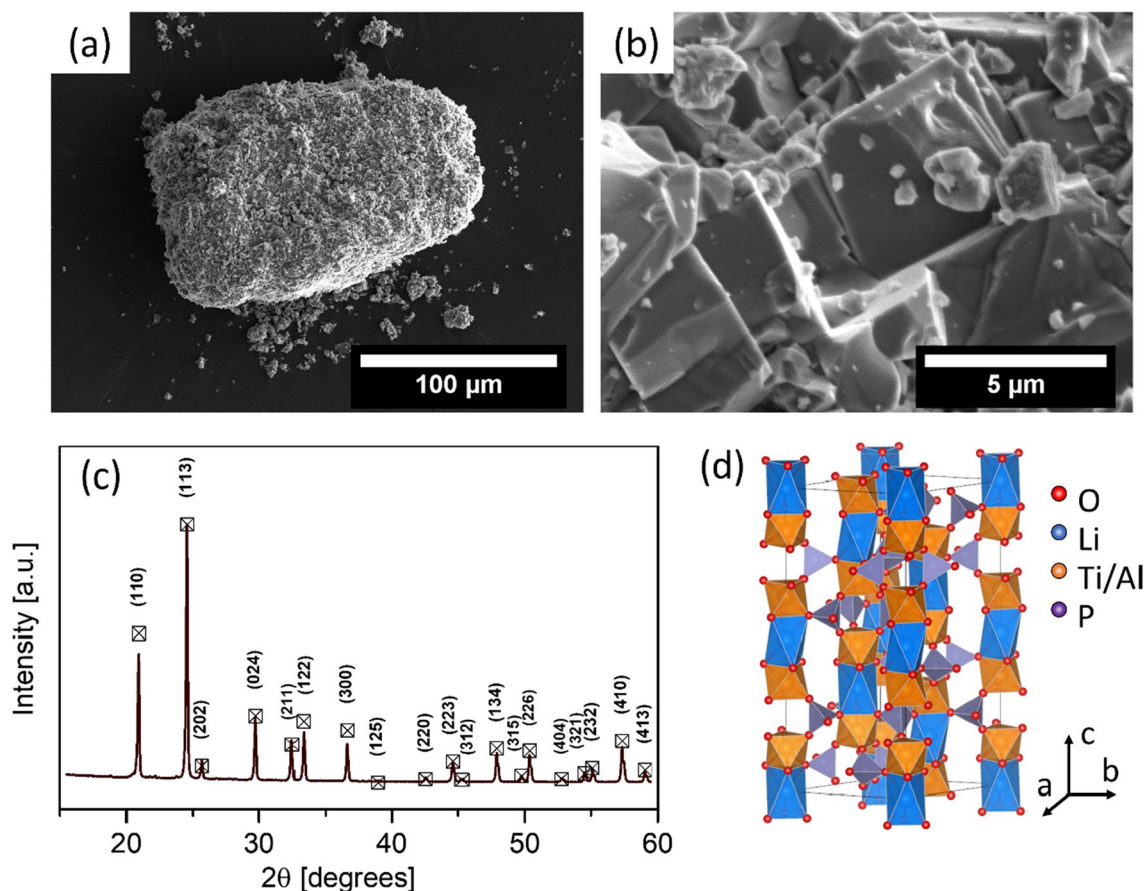


Figure 1: Scanning electron microscopy (SEM) micrographs of the as-received LATP powder showing (a) secondary and (b) primary powder particles. (c) X-ray diffraction (XRD) pattern of the as-received LATP powder (brown line) was indexed to the rhombohedral crystal structure (space group R-3c). Black squares show reference peak positions. (d) Model of the LATP crystal structure displays the oxygen atoms in red, the lithium atoms in blue, the titanium and aluminum atoms in orange, and the phosphorus atoms in purple.

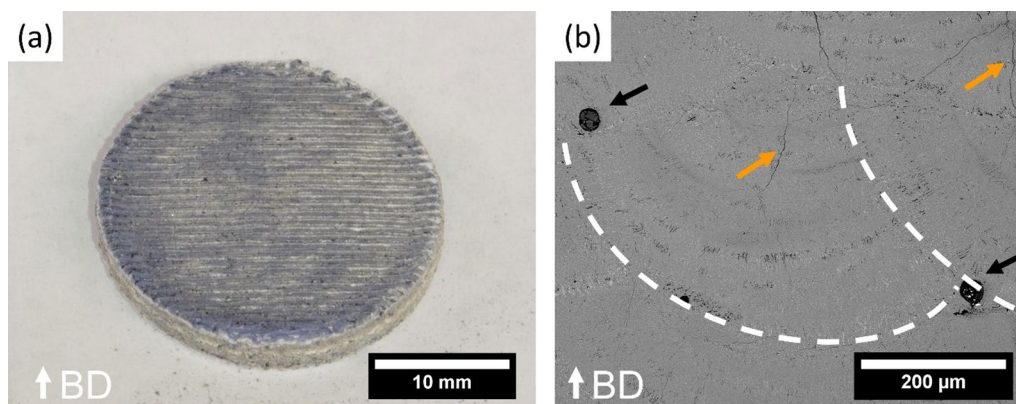


Figure 2: (a) Photograph of a representative as-prepared laser powder bed fusion LATP sample. (b) Scanning electron microscopy (SEM) micrograph of the polished cross-section reveals the typical clamshell shape of the solidified laser powder bed fusion melt pool (white dashed lines), cracks (orange arrows), and pores (black arrows). The build direction (BD) is identified by the white arrow in the bottom left.

TABLE 1: Relative density and average grain size of the laser powder bed fusion LATP samples.

Laser scan speed [mm s ⁻¹]	Relative density [%]	Average grain size [μm]
8.7	95.2 ± 16.4	0.96 ± 0.59
10.6	94.4 ± 1.4	0.73 ± 0.36
13.5	95.9 ± 5.2	1.58 ± 1.11

distribution of secondary phases (Fig. 3a) and crack propagation (Fig. 3b) within the columnar dendritic microstructure of the L-PBF LATP samples along the build direction. The dendrites are comprised of LATP, whereas the lighter gray-scale regions are titanium-rich, and the darker gray-scale regions are aluminum-rich (highlighted with white arrows in Fig. 3a). The STEM bright field micrograph, Fig. 3c, displays the cross-section of a dendrite. The STEM-EDS maps, Fig. 3d, reveal that oxygen (blue), phosphorus (pink), titanium (red), and aluminum (yellow) are present within the dendrite. The regions between the secondary dendrite arms are aluminum-rich and retain phosphorus and oxygen. The interdendritic regions are titanium-rich and retain oxygen but are deficient in aluminum and phosphorus. Figure 3b shows how the secondary phases influence crack propagation. The cracks propagate toward the darker gray-scale particles (highlighted by the white arrows) and then continue around the lighter gray-scale particles (highlighted by the white dashed circle).

XRD was used to determine the crystal structures of the secondary phases identified with SEM, STEM, and EDS. The rhombohedral crystal structure (with the R-3c space group) is the primary phase state of the AR-LATP powder and the L-PBF LATP samples (Fig. 4a). Additional diffraction peaks at 2θ values of 21.45°, 25.33°, and 27.45° correspond to the secondary phases AlPO_4 (ICSD PDF: 01-072-7638), anatase TiO_2 (ICSD PDF: 03-065-5714), and rutile TiO_2 (ICSD PDF: 00-021-1276),

respectively. The relative intensity ratios of the secondary phase diffraction peaks, displayed as the secondary phase content in Fig. 4b, exhibit higher variability for lower laser scan speed conditions. Higher values of laser scan speed produce less secondary phase and less variability in the L-PBF LATP samples.

We proceed by investigating the mechanical behavior of L-PBF LATP samples. Specifically, nanoindentation measurements were performed to determine how the presence of microstructural features, such as columnar dendritic grains and secondary phases, contribute to the mechanical behavior of the L-PBF LATP samples. The Young's modulus (E) and hardness (H) of the L-PBF LATP samples are displayed as a function of laser scan speed in Table 2. No monotonic relationship between laser scan speed and the mechanical properties of the L-PBF LATP samples can be established, yet the lowest laser scan speed, 8.7 mm s⁻¹, produces the highest Young's modulus and nano-hardness values. The 95% confidence interval is provided for all mechanical properties.

To understand the mechanisms governing secondary phase formation in L-PBF LATP, we employed X-ray photoelectron spectroscopy (XPS) to evaluate lithium concentration in the as-prepared samples. Formation of secondary phases in LATP is often associated with deviations from stoichiometric amounts of lithium that arise during high-temperature processing [2]. Lithium concentration as a function of laser scan speed is shown in Fig. 5a. The error bars in Fig. 5a represent the standard deviation from XPS measurements collected at different positions on the surface of each sample. While the lithium concentration in the L-PBF LATP samples is comparable with lithium concentration in stoichiometric LATP, $\text{Li}_{1.3}\text{Al}_{0.3}\text{Ti}_{1.7}(\text{PO}_4)_3$ (dashed line in Fig. 5a), the large variability in lithium concentration values indicates a heterogeneous distribution of lithium throughout the samples. The fraction of reduced titanium (Fig. 5b) was also evaluated using XPS to provide insight into the processing temperature achieved during

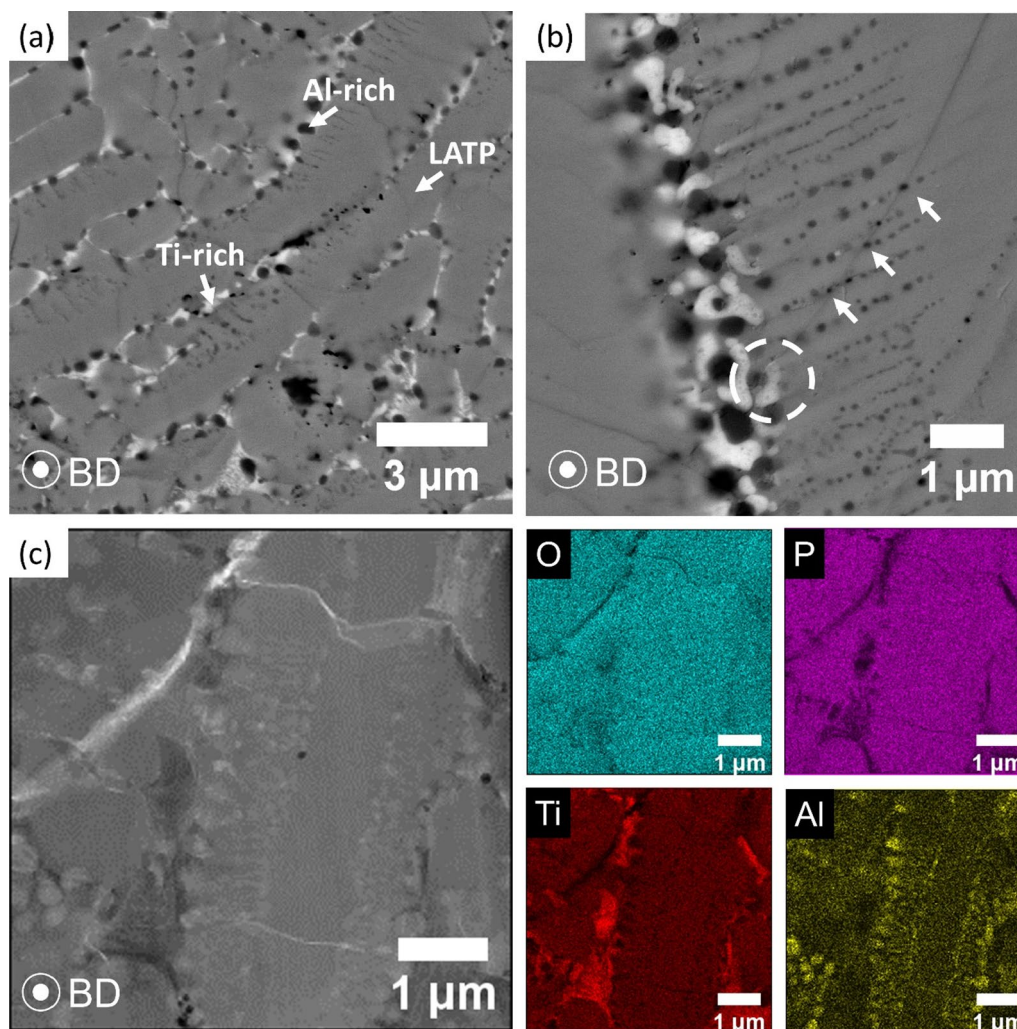


Figure 3: Backscattered scanning electron microscopy (BSE SEM) micrographs of a cross-sectioned and polished laser powder bed fusion LATP sample reveal: (a) the primary phase, LATP (medium gray-scale), secondary phases, titanium-rich (lighter gray-scale) and aluminum-rich (darker gray-scale), and (b) crack propagation. The arrows in (b) indicate crack propagation through aluminum-rich secondary phase particles (darker gray-scale) whereas the white dashed circle highlights crack deflection by a titanium-rich secondary phase particle (lighter gray-scale). (c) A scanning transmission electron microscopy (STEM) micrograph displaying the cross-section of a dendrite within a laser powder bed fusion LATP sample. STEM energy dispersive X-ray spectroscopy (EDS) maps of oxygen (blue), phosphorus (pink), titanium (red), and aluminum (yellow) reveal that regions between secondary dendrite arms are aluminum-rich (Al-rich) whereas the interdendritic regions are titanium-rich (Ti-rich) and deficient in phosphorus and aluminum. The build direction (BD) points out of the page for all micrographs.

L-PBF, since more extensive reduction likely occurs at higher temperatures. The extent of Ti^{4+} reduction to Ti^{3+} is provided by the atomic percent ratio of $\text{Ti}^{3+}/(\text{Ti}^{3+} + \text{Ti}^{4+})$ where a higher value indicates increased reduction of Ti^{4+} to Ti^{3+} (i.e., higher fraction reduced in Fig. 5b). The L-PBF LATP samples exhibit $\text{Ti}^{3+}/(\text{Ti}^{3+} + \text{Ti}^{4+})$ ratios, denoted as $\text{Ti}^{3+}/\text{Ti}_{\text{Total}}$ in Fig. 5b, of 0.58 ± 0.27 , 0.68 ± 0.12 , and 0.46 ± 0.11 for laser scan speed values of 8.7 mm s^{-1} , 10.6 mm s^{-1} and 13.5 mm s^{-1} , respectively. These values indicate that the L-PBF LATP sample produced using the highest laser scan speed undergoes the lowest amount of Ti^{4+} reduction.

The influence of the microstructure and heterogeneous distribution of lithium on ionic and electronic properties of the L-PBF LATP samples was characterized using electrochemical impedance spectroscopy (EIS) and chronoamperometry. The ionic conductivity and electronic conductivity values for the L-PBF LATP samples increase with increasing laser scan speed, whereas there is no monotonic trend between laser scan speed and dielectric constant values at 1 kHz, as displayed in Table 3. The highest laser scan speed produces the highest ionic conductivity value, $1.5 \times 10^{-8} \text{ S cm}^{-1}$. The electronic conductivity is several orders of magnitude lower than the ionic conductivity

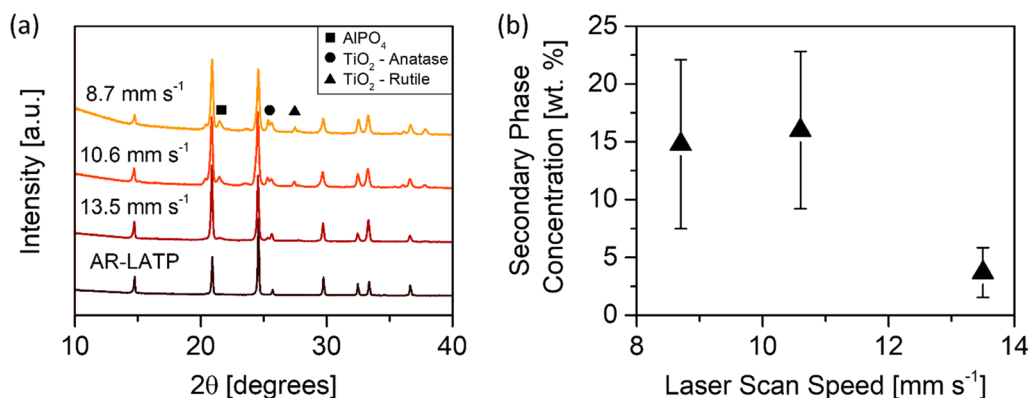


Figure 4: (a) X-ray diffraction (XRD) patterns for the as-received LATP (AR-LATP) powder and laser powder bed fusion LATP samples prepared using different laser scan speeds, 8.7 mm s⁻¹, 10.6 mm s⁻¹, and 13.5 mm s⁻¹. The primary phase of the laser powder bed fusion LATP samples matches the AR-LATP powder, while the secondary phases index to AlPO₄ (square data marker), anatase TiO₂ (circle data marker), and rutile TiO₂ (triangle data marker). (b) The concentration of secondary phases in the laser powder bed fusion LATP samples, determined by the relative intensity ratio method, is lowest for the highest laser scan speed. Error bars indicate standard deviations.

TABLE 2: Mechanical properties of the laser powder bed fusion LATP samples determined using nanoindentation measurements. The 95% confidence interval is provided.

Laser scan speed [mm s ⁻¹]	Young's modulus, E [GPa]	Hardness, H [GPa]
8.7	82.7 ± 2.9	7.1 ± 1.6
10.6	64.4 ± 3.1	6.0 ± 1.3
13.5	75.4 ± 2.0	6.1 ± 1.4

for all L-PBF LATP samples, which suggests the contribution of electrons to the total electrical conductivity is negligible.

The presence of secondary phases in conventionally prepared LATP samples is known to influence the electrical properties [1, 2]; however, the extent to which the secondary phases influence the electrical properties in our L-PBF LATP samples is unclear. It is expected that the electrical properties of the various phases, and the relative concentration of the phases, would contribute to the bulk conductive behavior in a mixed phase

material. Assuming that the electrical conductivity correlates exclusively with relative phase concentration and phase conductivity, the theoretical conductivity of our L-PBF LATP samples can be estimated using a rule of mixtures (RoM) relationship. Here, the RoM calculations utilized the concentration of secondary phases, determined using the XRD relative intensity ratio calculations shown in Fig. 4b, in conjunction with literature values of electrical properties for secondary phases in L-PBF LATP samples. Specifically, the influence of secondary phase concentration on the ionic conductivity and dielectric constant values of the L-PBF LATP samples was estimated. The RoM model assumes that the various phases in the L-PBF LATP samples are similar to their literature counterparts and are stoichiometric with minimal defects. The ionic conductivity values of the L-PBF LATP samples are several orders of magnitude lower than the crystalline and glass LATP RoM values (see Fig. 6a). The difference between the experimental ionic conductivity values for the L-PBF LATP samples and the RoM values indicates that the

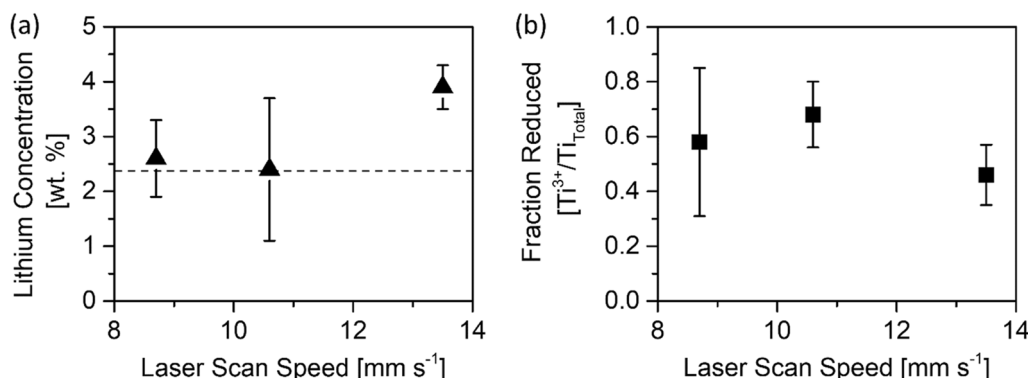


Figure 5: (a) Quantification of the lithium concentration, derived from X-ray photoelectron spectroscopy (XPS), is provided as a function of laser scan speed. The dashed line represents the concentration of lithium in theoretical LATP (Li_{1.3}Al_{0.3}Ti_{1.7}(PO₃)₄). (b) The amount of reduced titanium, Ti³⁺, is provided as the fraction of the total titanium, Ti_{Total} = Ti³⁺ + Ti⁴⁺, as a function of laser scan speed.

TABLE 3: Ionic conductivity, electronic conductivity, and dielectric constant at 1 kHz, derived from electrochemical impedance spectroscopy (EIS) data, for the laser powder bed fusion LATP samples as a function of laser scan speed.

Laser scan speed [mm s ⁻¹]	Ionic conductivity [S cm ⁻¹]	Electronic conductivity [S cm ⁻¹]	Dielectric constant at 1 kHz
8.7	1.5×10^{-10}	9.9×10^{-13}	6.6×10^4
10.6	2.0×10^{-9}	7.2×10^{-12}	1.1×10^4
13.5	1.5×10^{-8}	2.2×10^{-12}	4.2×10^3

concentration of secondary phases in the L-PBF LATP samples does not fully explain the measured ionic conductivity values. Conversely, the dielectric constant values of the L-PBF LATP samples at 1 kHz are larger than the RoM values that were based on literature values for crystalline LATP (see Fig. 6b), which suggests that the L-PBF LATP samples exhibit higher charge storage capabilities than conventional LATP. Further, the dielectric constant RoM results indicate that the amount of secondary phase in the L-PBF LATP samples does not explain the deviation in dielectric constant values from those for conventional LATP.

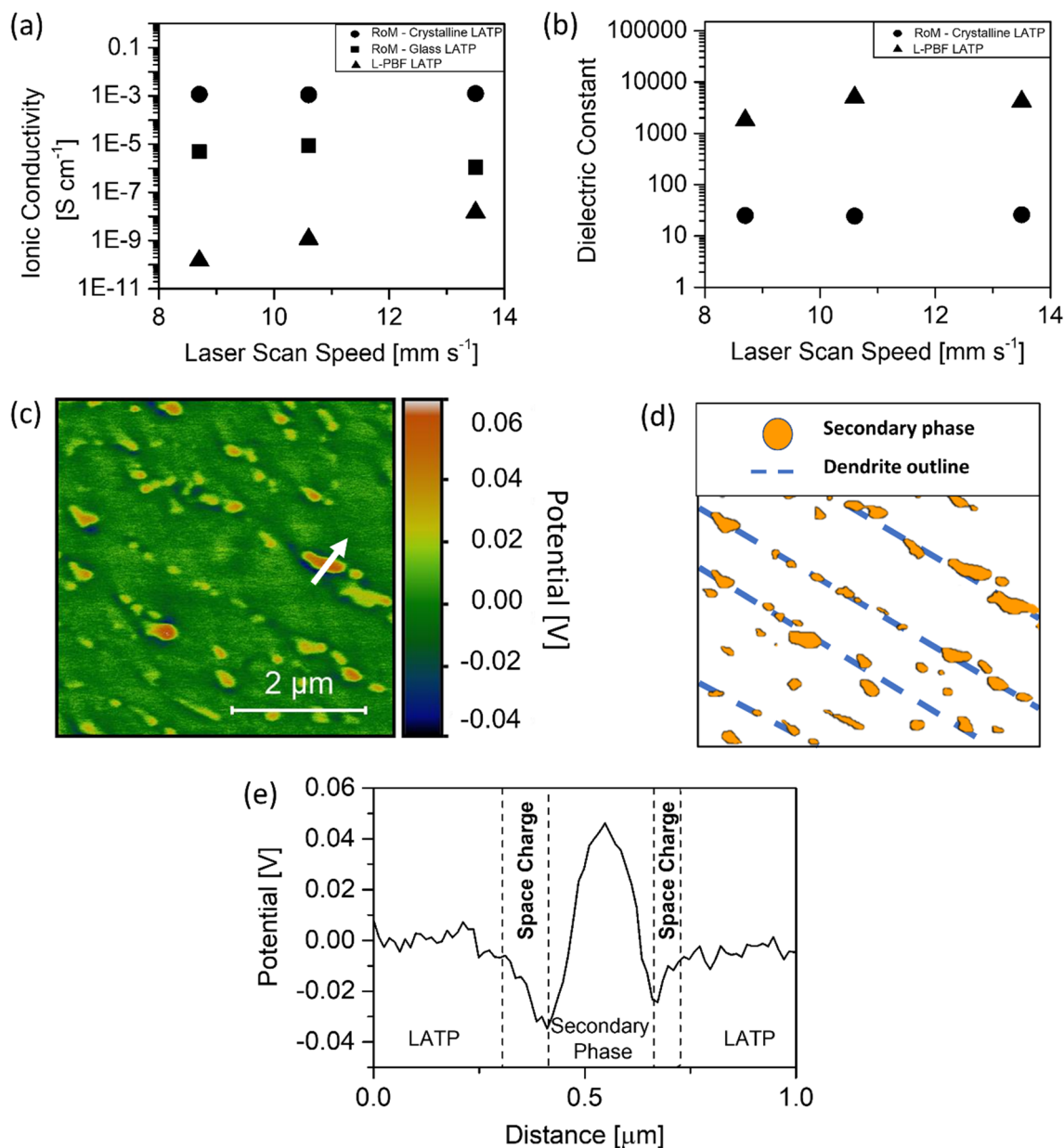


Figure 6: (a) Ionic conductivity and (b) dielectric constant values based on rule-of-mixture (RoM) calculations and experimental evaluation of the laser powder bed fusion (L-PBF) LATP samples. (c) A representative scanning Kelvin probe force microscopy (SKPFM) micrograph of a L-PBF LATP sample and (d) skeletonized version of the SKPFM micrograph that highlights the secondary phase particles in orange and approximately outlines the LATP dendrites with blue dashed lines. (e) The line profile results, from the white arrow indicated in the SKPRM micrograph in (c), reveal the space charge regions that are highlighted by the black dashed lines in (e).

The local influence of the secondary phases on functional properties is elucidated by scanning Kelvin probe force microscopy (SKPFM). A representative SKPFM micrograph of a L-PBF LATP sample is shown in Fig. 6c. The secondary phase particles (highlighted in Fig. 6d) exhibit higher potential values (0.041 ± 0.009 V), indicating a higher work function, than the LATP matrix phase (-0.003 ± 0.003 V). Further, the secondary phase particles exhibit a region within the LATP matrix phase with lower potential values indicative of a space charge region. On average, the space charge regions near secondary phase particles (Fig. 6e) are 123 ± 49 nm thick. The SKPFM micrograph reveals a heterogeneous distribution in the size and location of the secondary phase particles.

Discussion

Conventional preparation of LATP utilizes a two-stage glass–ceramic processing technique that employs the high cooling rates of splat-quenching to form a glass, then subjects the glass to secondary thermal processing (i.e., heat treatment) to develop a crystalline microstructure [1]. The crystalline microstructure of conventional LATP is commonly comprised of cubic shaped grains with secondary phases that develop at grain boundaries at temperatures above 1000 °C [1]. Although the similarity in cooling rates between L-PBF (10^3 – 10^4 K sec^{−1} [12]) and splat-quenching (10^4 – 10^{10} K sec^{−1} [21]) were expected to enable formation of glass LATP during L-PBF, the L-PBF LATP samples exhibit a columnar dendritic microstructure (Fig. 3a–c), which suggests that the microstructure developed directly from the melt-solidification process of L-PBF rather than undergoing the hypothesized two-stage microstructure development. Columnar dendritic grains commonly form in materials produced by L-PBF due to the highly localized heating and cooling phenomena of the high-energy laser beam that cause melting and directional solidification [22]. Since solidification proceeds parallel to the maximum thermal gradient, grains preferentially grow toward the laser-matter interaction zone (i.e., the top, center of the melt pool) normal to the melt pool boundary. The mode of solidification is determined by G/R, whereas the cooling rate (G*R) dictates the scale of the microstructural features. A coarse dendritic microstructure is commonly associated with lower cooling rates and lower G/R values [11]. Therefore, the presence of micron-scale columnar dendritic grains in the L-PBF LATP samples (Fig. 3a–c) indicates that relatively low G/R and cooling rate values were produced with the process parameters used in this study. The relatively low thermal conductivity of LATP, ~ 2 W/mK [23], likely contributes to the lower cooling rates and production of coarse dendritic microstructural features in the L-PBF LATP samples by limiting heat transfer.

Dendrite formation occurs due to constitutional supercooling. The temperature difference between the solidifying

dendrite tip and the liquidus temperature ahead of the dendrite tip provides the driving force for dendrite growth [22]. During dendritic solidification, the equilibrium phase solidifies first leading to the rejection of solute atoms into the liquid ahead of the dendrite tip [22]. The solute-rich liquid is last to solidify, resulting in the formation of secondary phase particles within the interdendritic regions. Therefore, the distribution of the secondary phase particles provides insight into the solidification timeline. The presence of aluminum-rich secondary phase particles (darker gray-scale in Fig. 3a) between the LATP secondary dendrite arms indicates that this phase solidifies before the titanium-rich secondary particles (lighter gray-scale in Fig. 3a). The presence of the titanium-rich secondary phase particles within interdendritic regions (Fig. 3c) indicates that this phase was last to solidify. The heterogeneous distribution of secondary phases in the L-PBF LATP samples is distinctly different from conventionally prepared LATP samples.

The differences in crystal structure between the LATP and the secondary phases can lead to microcrack formation and propagation [2]. Despite the different morphologies of the secondary phases, the crack propagation behavior in the L-PBF LATP samples (Fig. 3b) is consistent with that observed in conventional LATP, as described in the literature [2]. AlPO_4 serves as a stress concentrator that cracks propagate toward and through (highlighted by the white arrows in Fig. 3b), whereas TiO_2 impedes crack propagation and increases crack length (highlighted by the white dashed circle in Fig. 3b). The mechanical properties of the L-PBF LATP samples (Table 3) are also comparable to literature values for conventional LATP (Young's modulus: 81–115 GPa [3]).

Though the secondary phases do not significantly influence the mechanical behavior of the L-PBF LATP samples, production of single-phase LATP samples is desirable for energy storage applications since secondary phases are known to hinder ion transport and lower the ionic conductivity. The relationship between laser scan speed and secondary phase content (Fig. 4) suggests that further refinement of the laser scan speed may enable production of single-phase LATP samples using L-PBF.

The rhombohedral crystal structure is super ion conducting in conventionally processed LATP samples, with limitations in ion transport arising due to the formation of secondary phases [1, 24]. Though the L-PBF LATP samples primarily exhibit the desired rhombohedral crystal structure (Fig. 4a) with secondary phase concentrations (Fig. 4b) qualitatively comparable to conventional processing, the ionic conductivity values for the L-PBF LATP samples (1.49×10^{-8} – 1.50×10^{-10} S cm^{−1} shown in Table 3) are several orders of magnitude lower than conventionally prepared LATP ($\sim 10^{-3}$ S cm^{−1}) [1]. In addition to the presence of the secondary phases, lithium content, titanium oxidation state, microstructure, and presence of microcracks are known to affect the ionic conductivity of LATP [2]. Each of these are considered below.

The development of LATP as a solid-state electrolyte requires high ionic conductivity and extremely low (or negligible) electronic conductivity for utilization in solid-state batteries. Typically, the electronic conductivity in LATP samples is negligible compared to ionic conductivity [25]; however, the reduction of titanium from, Ti^{4+} to Ti^{3+} , during high-temperature processing of LATP increases the electronic contribution to the total conductivity [1]. The violet appearance of the L-PBF LATP samples (Fig. 2a) is consistent with previous reports of conventionally prepared LATP [1] and indicates that titanium has undergone reduction during L-PBF processing, as confirmed by XPS evaluation and quantification in this study (Fig. 5b). Titanium reduction in LATP, from Ti^{4+} to Ti^{3+} , results from the redox equilibrium reaction with oxygen: $4\text{Ti}^{4+} + 2\text{O}^{2-} \leftrightarrow 4\text{Ti}^{3+} + \text{O}_2$ [1, 26], and occurs in the L-PBF LATP samples due to the reducing argon environment and high-temperature processing of L-PBF. Therefore, chronoamperometry was used to delineate the ionic and electronic contributions to the total electrical conductivity and to confirm that ionic transport is occurring in the L-PBF LATP samples. Chronoamperometry results (Table 3) show that the electronic conductivity of the L-PBF LATP samples is at least two orders of magnitude lower than the ionic conductivity. As such, the electronic contribution to the total electrical conductivity is considered negligible, indicating that ionic transport dominates in the L-PBF LATP samples. The electronic conductivity values for the L-PBF LATP samples (6.7×10^{-12} – 9.9×10^{-13} S cm^{-1} in Table 3) are lower than the values reported for conventional LATP (1.2×10^{-8} S cm^{-1}) [25]. However, the two orders of magnitude difference between ionic conductivity and electronic conductivity is consistent with literature values for conventional LATP [25], which suggests that factors that influence the ionic conductivity also influence the electronic conductivity of the L-PBF LATP samples.

The concentration and distribution of lithium is known to influence the ionic conductivity of solid-state electrolytes [27, 28]. Though the lithium content in the L-PBF LATP samples (triangle data markers in Fig. 5a) is comparable to the expected lithium content found in theoretical $\text{Li}_{1.3}\text{Al}_{0.3}\text{Ti}_{1.7}(\text{PO}_4)_3$ (dashed line in Fig. 5a), the large standard deviation in lithium content indicates that lithium is heterogeneously distributed throughout the L-PBF LATP microstructure. The heterogeneous distribution of lithium arises from the presence of secondary phases, such as AlPO_4 and TiO_2 , that do not contain lithium and are expected to influence the ionic conductivity. The formation of secondary phases, AlPO_4 and TiO_2 , is common during high-temperature processing of LATP and typically results in decreased values of ionic conductivity [1, 2, 23]. Further, the amount of secondary phases increases with increases in processing temperature [1, 2, 23]. As such, the lower concentration of secondary phases when the highest laser scan speed is used (Fig. 4b) arises from

the influence of laser scan speed on the processing temperature during L-PBF. Higher laser scan speeds will impart less energy on the powder bed per unit length of material leading to lower processing temperatures than lower laser scan speeds [29]. Although not explored in the present study, laser power is known to influence processing temperature such that higher laser power leads to higher processing temperatures [29]. Therefore, it is expected that the concentration of secondary phases that develop in L-PBF LATP samples would increase with the implementation of higher values of laser power. The amount of secondary phase in L-PBF LATP has the potential to influence the ionic conductivity with higher secondary phase concentration leading to a heterogeneous lithium concentration and lower values of ionic conductivity.

RoM calculations were used to identify an upper bound for the effects that secondary phase content will theoretically have on ionic conductivity and dielectric constant. Since the microstructure of conventional LATP is known to alter the ionic conductivity by several orders of magnitude [1], the RoM values were determined using ionic conductivity values of both glass and crystalline LATP [1] to provide an estimated range of values for the L-PBF LATP samples. The values from the literature are for conventional crystalline LATP materials with an equiaxed grain morphology, which is different than the columnar dendritic grain morphology observed in L-PBF LATP. The ionic conductivity values from the RoM calculations do not significantly change with laser scan speed, indicating that a difference in secondary phase content of ~10 wt. % does not significantly influence the ionic conductivity. Therefore, the secondary phase content on its own does not explain the trend between ionic conductivity values and laser scan speed. Further, the ionic conductivity values of the L-PBF LATP samples do not fall between the crystalline and glass LATP RoM values, suggesting that crystallinity alone also does not account for the significantly lower ionic conductivity values in the L-PBF LATP samples relative to conventionally prepared LATP. The disagreement between RoM ionic conductivity values and that of the L-PBF LATP samples may, however, arise from the significant difference in grain morphology, as discussed below.

RoM calculations for dielectric constant were also performed to determine whether secondary phase content explains the increased polarization in the L-PBF LATP samples. The dielectric constant correlates to the capacitive behavior, which may elucidate alternative charge transport mechanisms in the L-PBF LATP samples. The L-PBF LATP samples exhibit dielectric constant values that are at least an order of magnitude higher than the RoM dielectric constant values (Fig. 6b). Further, the RoM dielectric constant values do not significantly change as secondary phase content changes (Fig. 4b). The significant difference between the dielectric constant values for L-PBF LATP and the RoM calculations indicates that secondary phase content does

not explain the higher dielectric constant values for the L-PBF LATP samples. Further, the L-PBF LATP dielectric constant values at a frequency of 1 kHz are two orders of magnitude larger than that for conventionally prepared LATP [30]. These higher dielectric constant values indicate that increased polarization occurs in the L-PBF LATP samples, but they cannot be fully explained by the content of secondary phases.

The microstructure of the L-PBF LATP samples likely contributes to the discrepancy in ionic conductivity and dielectric constant values, compared to conventionally prepared LATP. For instance, formation of columnar dendritic grains leads to a heterogeneous distribution of secondary phases and lithium content throughout the L-PBF LATP microstructure (Fig. 3a and Fig. 5). The Kelvin-probe-determined potentials for the secondary phase particles (Fig. 6e) are more than double that of the LATP matrix phase, which indicates that the secondary phase particles have a higher work function. Higher work function has previously been associated with decreased concentrations of lithium in solid-state battery materials [31], which is consistent with the chemical composition of the secondary phases in the L-PBF LATP samples. Since the ionic conductivity of solid-state electrolytes depends on lithium concentration [27], the heterogeneous distribution of lithium is expected to hinder ion transport and lower the ionic conductivity of the L-PBF LATP samples. Further, lithium deficient regions and interfaces near the secondary phase particles likely contribute to the development of the 122 ± 58 nm space charge region observed in the L-PBF LATP samples (Fig. 6e). Recent studies show that space charge effects can lead to significantly lower ionic conductivity values in all-solid-state batteries [32]. Specifically, the presence of space charge regions that arise from lithium deficiencies in LATP samples is known to increase polarization and impedance, which is expected to result in higher dielectric constant values and lower ionic conductivity values [28]. Our results therefore suggest that the heterogeneous distribution of secondary phases and lithium due to the formation of a columnar dendritic microstructure leads to increased polarization and decreased ionic conductivity in the L-PBF LATP samples.

Conclusions

L-PBF produces relatively dense LATP samples (up to ~96% dense) that primarily exhibit the super ion conducting rhombohedral crystal structure. Although average grain size and mechanical properties are comparable to conventionally prepared LATP [3], the columnar dendritic grain morphology leads to a unique distribution of secondary phase particles that segregate to interdendritic regions and influence the electrical properties of ionic conductivity, electronic conductivity, and dielectric constant. The heterogeneous distribution of secondary phases and lithium lower the overall magnitude of ionic conductivity

values of the L-PBF LATP samples compared to literature values of conventionally prepared LATP samples. However, increasing the laser scan speed produces less secondary phase resulting in lower microstructural heterogeneity, which increases the ionic conductivity. The correlation between laser scan speed and ionic conductivity suggests that further improvements in performance are possible through additional refinement of L-PBF process parameters.

Methods

Commercially available, AR-LATP powder (NEI Corporation, Somerset, NJ, USA), with 53–106 μm diameter particles, was used as the feedstock material for this study. The particle morphology and phase state of the AR-LATP powder was characterized using SEM (FEI Magellan 400 XHR SEM) and XRD (Rigaku SmartLab X-ray Diffractometer with D/teX Ultra), respectively. Using a Cu K α X-ray source, the XRD data were collected from 10° – 85° using a scan speed of 4.00 $^\circ/\text{minute}$ with a step width of 0.02° . The relative intensity ratio method [33] for calculating phase fractions was performed on the XRD data using the Rigaku PDXL Integrated X-ray powder diffraction software. The crystal structure of the AR-LATP powder was modeled using the Vesta software [34].

The L-PBF LATP samples were fabricated using a custom-built powder bed setup in an Optomec LENS[®] 750 Workstation. AR-LATP powder was manually spread onto an alumina substrate using a flat-edge spatula. The 1 kW top-hat fiber laser was defocused using a working distance of 16.3 mm to produce a laser beam diameter of 0.60 mm. The laser beam diameter was experimentally determined for this LENS[®] system in a previous study [35]. The laser beam was rastered over the powder bed according to the two-dimensional slice of a three-dimensional CAD model. After deposition of each layer, the z-height of the laser head (i.e., along the build direction) was increased by 100 μm to accommodate a fresh bed of powder. Three-dimensional L-PBF LATP cylinders (\varnothing 25 mm \times 16 layers) were prepared using a laser beam diameter of 0.60 mm, laser power of 100 W, and three different laser scan speeds, 8.7 mm s^{-1} , 10.6 mm s^{-1} , and 13.5 mm s^{-1} . The L-PBF LATP samples were prepared using a layer thickness of ~100 μm , a snake laser scan pattern, a 40% hatch overlap, and a 45° hatch rotation.

The density of the polished L-PBF LATP samples was determined using the Archimedes method. The relative density was calculated based on the theoretical density, 2.947 g cm^{-3} , of phase pure LATP [3]. The relative density of at least three samples was determined and averaged for each laser scan speed.

The average grain size and secondary phase morphology were characterized using SEM. The grain size was determined using fracture surfaces. To assess the secondary phase morphology, the L-PBF LATP samples were cross-sectioned along the

build direction using a diamond blade slow-speed saw, polished (70 μm , 30 μm , 15 μm , 6 μm , 1 μm diamond slurry), and coated with 1.5 nm of Ir (Leica ACE600 Sputter Coater) for SEM evaluation. Micrographs were collected using backscattered electrons during SEM.

STEM (JEOL JEM-2800 TEM) and EDS (Dual 100 mm² Silicon Drift Detectors) were performed on the FIB lift out lamella from the L-PBF LATP sample prepared using a laser scan speed of 8.7 mm s⁻¹. To prepare the STEM sample, Pt was first deposited using an accelerating voltage of 30 kV and current of 175 pA. Trenching was performed using an accelerating voltage of 30 kV and current of 19 nA, followed by successive polishing at 30 kV and 2 nA, 30 kV and 600 pA, 15 kV and 150 pA, and finally 3 kV and 90 pA. STEM/EDS evaluation was performed on the STEM sample using an accelerating voltage of 200 kV.

The phase state was determined by performing XRD on the top surface of the as-prepared L-PBF LATP samples. Prior to XRD evaluation, the as-prepared L-PBF LATP samples were rinsed with isopropanol to remove loose powder particles that had attached to the sample from the powder bed.

Nanoindentation (Agilent G200 Nanoindenter) was performed on the polished L-PBF LATP samples to determine the Young's modulus and hardness. Using a Berkovich indenter tip, the samples were subject to a maximum load of 100 mN with a constant loading rate of 1 mN s⁻¹ and held at the maximum load for 50 s before unloading. Over 100 indents were performed on each sample. The Young's modulus and hardness were calculated from the nanoindentation load-displacement curves using methods by Oliver and Pharr [36] and Fischer-Cripps [37]. The Poisson's ratio was set to 0.26 for all calculations based on values from a similar solid-state electrolyte ceramic material [38].

The chemical composition of the samples was evaluated using XPS (Kratos Analytics Axis Supra). The Al K α X-ray source was set to an emission current of 20 mA and an X-ray power of 300 W. Detailed XPS spectra were collected using a resolution of 20 eV. The charge neutralizer was used for all data collection. The data were analyzed using CasaXPS software [39]. All binding energies were charge corrected by calibrating the adventitious C 1 s peak to 284.8 eV.

EIS (Solartron SI 1287 Electrochemical Interface) measurements were performed using a two-probe cell to determine the electrical conductivity with contributions from electrons and ions. The L-PBF LATP samples were thinned along the laser scan direction to a thickness of 0.5 mm and polished to 15 μm diamond slurry. Silver (Ag) paste was applied as the ion blocking electrodes in an Ag/LATP/Ag configuration. To mitigate atmospheric effects during EIS measurements, the Ag-coated L-PBF LATP samples were dried at 130 °C in a vacuum furnace overnight and packaged in a pouch cell sleeve under an argon environment. During EIS measurements, a 20 mV AC perturbation was applied across the frequency

range, 0.5 Hz to 1 MHz. The electronic conductivity was determined using chronoamperometry with a bias of 0.2 V. The electronic contribution to current (I_e) was derived from the time-independent current region which occurs after the initial drop in current and once the values reach a steady state. The electronic conductivity was calculated using electronic resistance derived from Ohm's law, $V = I_e R$. The ionic conductivity was determined by subtracting the electronic conductivity from the total electrical conductivity that was experimentally determined from EIS. The electrical conductivity was established using an equivalent circuit with a resistor in parallel with a constant phase element that are in series with a Warburg element. The dielectric constant was calculated by determining the geometric capacitance from the imaginary impedance values at 1 kHz.

RoM calculations [40] were performed to estimate the influence of secondary phase content, derived from XRD relative intensity ratio methods [33], on the ionic conductivity and dielectric constant values of conventionally prepared LATP from literature. The equation used to determine the RoM values for both ionic conductivity and dielectric constant is $\gamma_{Th} = \gamma_1 W_1 + \gamma_2 W_2 + \gamma_3 W_3 + \dots$ [40] where γ is the literature value for either ionic conductivity or dielectric constant and W is the weight fraction for each phase identified from the XRD relative intensity ratio results. The ionic conductivity values from literature are 1.10×10^{-9} S cm⁻¹, 1.3×10^{-3} S cm⁻¹, 1.00×10^{-6} S cm⁻¹, 1.50×10^{-5} S cm⁻¹, and 8.54×10^{-5} S cm⁻¹ for glass Li_{1.3}Al_{0.3}Ti_{1.7}(PO₄)₃ [1], crystalline Li_{1.3}Al_{0.3}Ti_{1.7}(PO₄)₃ [1], rutile TiO₂ [41], anatase TiO₂ [42], and AlPO₄ [43], respectively. The dielectric constant values from literature are 25, 114, 31, and 4.5 for Li_{1.3}Al_{0.3}Ti_{1.7}(PO₄)₃ [30], rutile TiO₂ [41], anatase TiO₂ [41], and AlPO₄ [43], respectively.

SKPFM (Anton Paar Tosca 400 AFM) was performed to evaluate the local contact potential. The feedback control gain was set to 100. The horizontal resolution was 400 with an acquisition rate of 1 line/second. To obtain the SKPFM data, the frequency was set to 76.03 kHz with a phase offset of 167.8° and a drive of 100%. The AC excitation was held constant at 5 V with a SKPFM current gain of 5000 and a potential gain of 4. The average of five line profiles was used to determine the average potential values for LATP and secondary phases, as well as the average length of the space charge region.

Acknowledgments

This work was supported by a NASA Space Technology Graduate Research Opportunities Fellowship, Grant No. 80NSSC18K1146. ADD and JMS acknowledge partial support from the National Science Foundation (Grant NSF-CMMI-2029966). XW and ALV acknowledge support from UCI. The authors acknowledge the use of facilities and

instrumentation at the UC Irvine Materials Research Institute (IMRI), which is supported in part by the National Science Foundation through the UC Irvine Materials Research Science and Engineering Center (DMR-2011967). XPS was performed using instrumentation funded in part by the National Science Foundation Major Research Instrumentation Program under grant no. CHE-1338173. Part of the research was carried out at the Jet Propulsion Laboratory, California Institute of Technology, under a contract with the National Aeronautics and Space Administration (80NM0018D0004).

Data availability

The datasets generated during and/or analyzed during the current study are available from the corresponding author on reasonable request.

Declarations

Conflict of interest On behalf of all authors, the corresponding author states that there is no conflict of interest.

References

1. J.L. Narváez-Semanate, A.C.M. Rodrigues, Solid State Ionics (2010). <https://doi.org/10.1016/j.SSI.2010.05.010>
2. K. Waetzig, A. Rost, U. Langklotz, B. Matthey, J. Schilm, J. Eur. Ceram. Soc. (2016). <https://doi.org/10.1016/j.jeurceramsoc.2016.02.042>
3. S.D. Jackman, R.A. Cutler, J. Power Sources. (2012). <https://doi.org/10.1016/j.jpowsour.2012.06.081>
4. S. Yu, R.D. Schmidt, R. Garcia-Mendez, E. Herbert, N.J. Dudney, J.B. Wolfenstine, J. Sakamoto, D.J. Siegel, Chem. Mater. (2016). <https://doi.org/10.1021/acs.chemmater.5b03854>
5. H. Yves-Christian, W. Jan, M. Wilhelm, W. Konrad, P. Reinhart, Phys. Procedia. (2010). <https://doi.org/10.1016/j.phpro.2010.08.086>
6. F. Niu, D. Wu, G. Ma, J. Wang, M. Guo, B. Zhang, Scr. Mater. (2015). <https://doi.org/10.1016/j.scriptamat.2014.09.026>
7. F. Niu, D. Wu, G. Ma, S. Zhou, B. Zhang, Rapid Prototyp. J. (2015). <https://doi.org/10.1108/RPJ-12-2014-0167>
8. F. Niu, D. Wu, F. Lu, G. Liu, G. Ma, Z. Jia, Ceram. Int. (2018). <https://doi.org/10.1016/j.ceramint.2018.05.036>
9. L. Fu, X. Fu, G. Chen, W. Han, W. Zhou, Scr. Mater. (2017). <https://doi.org/10.1016/j.scriptamat.2016.10.024>
10. Z. Fan, Y. Zhao, Q. Tan, N. Mo, M.X. Zhang, M. Lu, H. Huang, Acta Mater. (2019). <https://doi.org/10.1016/j.actamat.2019.03.020>
11. T. DebRoy, H.L. Wei, J.S. Zuback, T. Mukherjee, J.W. Elmer, J.O. Milewski, A.M. Beese, A. Wilson-Heid, A. De, W. Zhang, Prog. Mater. Sci. (2018). <https://doi.org/10.1016/j.pmatsci.2017.10.001>
12. B. Zheng, Y. Zhou, J.E. Smugeresky, J.M. Schoenung, E.J. Lavernia, Metall. Mater. Trans. A. (2008). <https://doi.org/10.1007/s11661-008-9557-7>
13. K.C. Datsiou, E. Saleh, F. Spirrett, R. Goodridge, I. Ashcroft, D. Eustice, J. Am. Ceram. Soc. (2019). <https://doi.org/10.1111/jace.16440>
14. M. Pang, R. Suzuki, M. Saito, K. Machida, H. Hanzawa, Y. Nojiri, S. Tanase, Appl. Phys. Lett. (2008). <https://doi.org/10.1063/1.2838355>
15. B. Almangour, Additive Manufacturing of Emerging Materials. Springer (2018). <https://doi.org/10.1007/978-3-319-91713-9>
16. H. Choo, K.L. Sham, J. Bohling, A. Ngo, X. Xiao, Y. Ren, P.J. Depond, M.J. Matthews, E. Garlea, Mater. Des. (2019). <https://doi.org/10.1016/j.matdes.2018.12.006>
17. W. Kurz, B. Giovanola, R. Trivedi, Acta Metall. (1986). [https://doi.org/10.1016/0001-6160\(86\)90056-8](https://doi.org/10.1016/0001-6160(86)90056-8)
18. Q. Jia, D. Gu, J. Alloys Compd. (2014). <https://doi.org/10.1016/j.jallcom.2013.09.171>
19. A. Aatiq, M. Ménétrier, L. Croguennec, E. Suard, C. Delmas, J. Mater. Chem. (2002). <https://doi.org/10.1039/b203652p>
20. J.J. Lewandowski, M. Seifi, Annu. Rev. Mater. Res. (2016). <https://doi.org/10.1146/annurev-matsci-070115-032024>
21. R.C. Ruhl, Mater. Sci. Eng. (1967). [https://doi.org/10.1016/0025-5416\(67\)90013-4](https://doi.org/10.1016/0025-5416(67)90013-4)
22. D.A. Porter, K.E. Easterling, M.Y. Sherif, Phase Transformations in Metals and Alloys, CRC Press, 1980.
23. E.C. Bucharsky, K.G. Schell, T. Hupfer, M.J. Hoffmann, M. Rohde, H.J. Seifert, Ionics (Kiel). (2016). <https://doi.org/10.1007/s11581-015-1628-3>
24. A. Mertens, S. Yu, N. Schön, D.C. Gunduz, H. Tempel, R. Schierholz, F. Hausen, H. Kungl, J. Granwehr, R.A. Eichel, Solid State Ionics (2017). <https://doi.org/10.1016/j.SSI.2017.07.023>
25. E. Zhao, F. Ma, Y. Jin, K. Kanamura, J. Alloys Compd. (2016). <https://doi.org/10.1016/j.jallcom.2016.04.173>
26. W.D. Johnston, J. Am. Ceram. Soc. (1964). <https://doi.org/10.1111/j.1151-2916.1964.tb14392.x>
27. B. Kozinsky, S.A. Akhade, P. Hirel, A. Hashibon, C. Elsässer, P. Mehta, A. Logeat, U. Eisele, Phys. Rev. Lett. (2016). <https://doi.org/10.1103/PhysRevLett.116.055901>
28. N.J.J. De Klerk, M. Wagemaker, A.C.S. Appl. Energy Mater. (2018). <https://doi.org/10.1021/acsaem.8b01141>
29. V. Manvatkar, A. De, T. DebRoy, Mater. Sci. Technol. (2015). <https://doi.org/10.1179/1743284714Y.00000000701>
30. T. Zangina, J. Hassan, K.A. Matori, R.S. Azis, U. Ahmadu, A. See, Results Phys. (2016). <https://doi.org/10.1016/j.rinp.2016.10.003>
31. K. Yamamoto, Y. Iriyama, T. Asaka, T. Hirayama, H. Fujita, C.A.J. Fisher, K. Nonaka, Y. Sugita, Z. Ogumi, Angew. Chem. Int. Ed. (2010). <https://doi.org/10.1002/anie.200907319>

32. Z. Cheng, M. Liu, S. Ganapathy, C. Li, Z. Li, X. Zhang, P. He, H. Zhou, M. Wagemaker, *Joule* (2020). <https://doi.org/10.1016/j.joule.2020.04.002>
33. R.L. Snyder, *Powder Diffr.* (1992). <https://doi.org/10.1017/S0885715600018686>
34. Koichi Momma, F. Izumi, *J. Appl. Phys.* (2008). <https://jp-minerals.org/vesta/en/>. Accessed December 18, 2020.
35. K. Acord, A. Dupuy, U.S. Bertoli, B. Zheng, W. West, Q.N. Chen, A. Shapiro, J. Schoenung, *J. Mater. Process. Technol.* (2020). <https://doi.org/10.1016/j.jmatprotec.2020.116827>
36. W.C. Oliver, G.M. Pharr, *J. Mater. Res.* (1992). <https://doi.org/10.1557/JMR.1992.1564>
37. A.C. Fischer-Cripps (2013). http://www.fclabs.com.au/index_html_files/IBIS_HandbookOfNanoindentationBook.pdf. Accessed October 15, 2019.
38. J.E. Ni, E.D. Case, J.S. Sakamoto, E. Rangasamy, J.B. Wolfenstine, *J. Mater. Sci.* (2012). <https://doi.org/10.1007/s10853-012-6687-5>
39. C.S. Ltd. (2005). <http://www.casaxps.com/>. Accessed November 23, 2020.
40. Y.M. Chiang, D.P. Birnie, W.D. Kingery, *Physical Ceramics*, J. Wiley, 1997.
41. L.J. Berberich, M.E. Bell, *J. Appl. Phys.* (1940). <https://doi.org/10.1063/1.1712721>
42. M.L. Sushko, K.M. Rosso, J. Liu, *J. Phys. Chem. C.* (2010). <https://doi.org/10.1021/jp107982c>
43. M.C. Record, A. Goiffon, J.C. Giuntini, E. Philippot, *J. Mater. Sci. Lett.* (1990). <https://doi.org/10.1007/BF00722162>